Research on the operation strategies of the solar assisted heat pump with triangular solar air collector

Yan Jiang [a, c], Huan Zhang [a, c], Yeming Wang [a, c], Yaran Wang [a, c, *], Minzhang Liu [b, *], Shijun You [a, c], Zhangxiang Wu [a, c], Man Fan [a], Shen Wei [d]

[a] School of Environmental Science and Engineering, Tianjin University, Haihe Education Area, Jinnan District, Tianjin 300350, PR China

[b] School of Energy and Safety Engineering, Tianjin Chengjian University, Tianjin 300384, PR China

[c] Tianjin Key Lab of Biomass/Wastes Utilization, Tianjin 300350, PR China

[d] The Bartlett School of Construction and Project Management, University College London (UCL), 1-19 Torrington Place, London WC1E 7HB, United Kingdom

Abstract

The solar-assisted heat pump (SAHP) is considered to be one of the efficient and promising clean heating technologies, while the research on its operation strategy is insufficient. In this study, a novel triangular solar air collector assisted air source heat pump (TSAHP) for rural residence heating is presented. Three working modes of the TSAHP including preheating, series and parallel modes were investigated, and corresponding mathematical models were established and verified. The effects of solar irradiance, outdoor temperature, indoor temperature, south wall covered area of the TSAC and the heating load on the performances of the three working modes were

[*] *Corresponding author. Tel.: +8602227892626; fax: +8602227892626.*

E-mail addresses: yaran_wang@tju.edu.cn

[*] *Corresponding author. Tel.: +8602227892626; fax: +8602227892626.*

E-mail addresses: liuminzhang@tju.edu.cn

analyzed. The distribution diagram of the optimal working mode was designed, and the equations that define the boundaries between operating modes were fitted. Finally, the performances of the TSAHP under typical meteorological parameters were compared and analyzed based on the modified boundary equations. Results indicate that the TSAHP can sufficiently utilize solar energy. With the increase of solar irradiance, the optimal working mode is shifted from the preheating to series and parallel. Compared with the traditional air source heat pump system, the COP of the TSAHP under the optimal working modes could be increased by 64.4%.

Keywords:

solar air collector; solar assisted heat pump; operation strategy; heat transfer model

Nomenclature

A	surface area (m^2)
C	heat capacity (W/K)
c_p	specific heat capacitance (J/(kg·K))
D	hole aperture of perforated corrugated absorber (m)
d	thickness (m)
d_{in}	inner diameter (m)
d_{out}	outer diameter (m)
f_{comb}	compressor frequency (Hz)
G	mass velocity ($kg/m^2/s$)
g	acceleration of gravity (m/s^2)
h_{conv}	convective heat transfer coefficient ($W/m^2/K$)
h_{rad}	radiative heat transfer coefficient ($W/m^2/K$)
I	solar irradiance (W/m^2)
i	refrigerant enthalpy (J/kg)
i_{lv}	refrigerant enthalpy from saturated liquid to saturated vapor (J/kg)
k	heat conductivity coefficient (W/m/K)

Subscripts

ab	perforated corrugated absorber
air	recirculation air of TSAC
comb	compressor
fan	fan of evaporator and condenser
gc	glass cover
ho	insulation housing of TSAC
hole	hole of perforated corrugated absorber
id	indoor
od	outdoor
ref	refrigerating fluid
sph	refrigerant single-phase region
tph	refrigerant two-phase region

Greek symbols

α	absorptivity (-)
β	inclination angle (°)
ε	emissivity (-)
η_{comb}	total compressor efficiency (%)
η_v	volume efficiency (%)
κ	Isentropic exponent (-)
λ	resistance factor (-)

L	length (m)	μ_{avg}	average dynamic viscosity of refrigerant (m^2/s)
m	mass flow rate (kg/s)	ρ_{avg}	average density (kg/m^3)
P	pressure (Pa)	ρ	density (kg/m^3)
P_h	porosity factor of perforated corrugated absorber (-)	ρ_κ	refrigerant density at the inlet entropy and outlet pressure of compressor (kg/m3)
Q_{conv}	convective heat transfer (W)		
Q_h	heating load of rural residence (W)		
Q_{rad}	radiant heat transfer (W)	ω	fan speed (rpm)
Q_{sol}	absorbed solar irradiance (W)	*Abbreviations*	
Q_u	net heat gain of TSAC (W)	SAC	solar air collector
T	temperature (℃)	SAHP	solar assisted heat pump
U	overall heat transfer coefficient ($W/m^2/K$)	WSAHP	solar hot water collector assisted heat pump
v	specific volume (m^3/kg)	ASAHP	solar air collector assisted heat pump
W	input power (W)	ASHP	air source heat pump
W_t	total input power (W)	TSAC	triangular solar air collector
Δx	difference of vapor quality (kg/kg)	TSAHP	triangular solar air collector assisted air source heat pump
y	heat transfer area percentage (%)		

1. Introduction

In China, about 65% of rural residence require heating in winter, while most of them still rely on burning raw coal, which consumed nearly 110 million tons in 2018 alone [1]. Burning large amounts of raw coal leads to serious environmental pollution such as particulate matter and carbon emissions. Traditional coal-fired heating is gradually replaced by clean heating technologies [2]. The heat pump is one of the most prospective measures in clean heating [3], and the solar-assisted heat pump (SAHP) can operate more efficiently, which is considered to be a promising heating technology in the near future [4].

The SAHP technology can be categorized as direct expansion type (DX-SAHP) and indirect expansion type (IX-SAHP) [5]. The DX-SAHP absorbs solar radiation directly through the collector/evaporator, while the IX- SAHP receives solar radiation

from the solar collector and then transfers heat to the evaporator. The DX-SAHP has been widely researched due to its high efficiency and compact unite. The collector/evaporator is the most critical component of the DX-SAHP [6]. Ma et al. [7] optimized the structure and material of the collector/evaporator by CFD method, the results show that the optimal thickness of the collector/evaporator fin is 4 mm, and the material is aluminum. Song et al. [8] developed a hybrid compound parabolic concentrator/photovoltaic/fin evaporator to improve the performance of DX-SAHP under low or no solar irradiance. Hao [9] et al. proposed a novel collector/evaporator as the heat absorber, and different operation control strategies of the DX-SAHP were studied. The major disadvantage of the collector/evaporator is that the air source utilization is weakened and the performance is reduced in low solar radiation [10]. Cai et al. [5] connected a finned tube evaporator in the DX-SAHP system to improve the utilization of air source, and the average COP was 2.71 when the solar radiation was 100 W/m^2. Liu et al. [11] jointed the evaporator and the collector/evaporator in parallel, and controlled the refrigerant flow distribution to achieve the high performance of the DX-SAHP system under different solar radiation. Connecting an additional evaporator in the DX-SAHP system can improve the comprehensive utilization of solar radiation and air source, while the system complexity and high initial cost make it unsuitable for rural residence heating.

Solar hot water collector assisted heat pump (WSAHP) is one of the main types of IX-SAHP, which has a good energy saving effect [12]. Agrebi et al. [13] compared the WSAHP to a traditional heat pump used to heat a 100 m^2 greenhouse and the WSAHP

could save more than 18% of the electrical energy consumption. Simonetti et al. [14] added supercooled phase change materials to the WSAHP system, and the daily energy consumption was reduced around 12.1% and 13.5% by controlling the heat release time of PCM. In addition, as solar hot water collector and heat pump have various coupling modes, it is necessary to study the operation strategy of the WSAHP system. Long et al. [15] analyzed the energy efficiency of the WSAHP system under the series, parallel and preheating modes, and calculated the optimal operating region for the three modes. Cai et al. [16] calculated the energy efficiency of the WSAHP system under the different working modes, and the COP was above 2.0 throughout the year with the optimal working strategy.

Compared with the WSAHP system, solar air collector (SAC) assisted heat pump (ASAHP) has the following advantages: (1) In the existing rural residences the air source heat pump (ASHP) is usually adopted, and the solar hot water collector coupled with the ASHP needs to modify evaporator into liquid-liquid heat exchanger or add liquid-air heat exchanger before the evaporator. The commercially available ASHP system can be easily integrated with the SACs with few modifications for rural residence application [17]. (2) The SAC can avoid the freezing problem that may occur in the solar hot water systems of the cold region. (3) WSAHP systems are expensive, difficult to install and take up more space [18]. Treichel and A.Cruickshank [17] deemed that the water-type solar collector was intrusive to the ASHP, and ASAHP was desirable for residential heating. Kegel et al. [19] presented an evaluation of the SAHP system for single detached residential houses, and the air type SAHP demonstrated

better energy savings and lower capital costs than water type SAHP in all housing types. Xu et al. [20] studied the performance of the ASAHP in severe cold regions, and the results showed that the COP reached 3.0 in regions, where the calculated heating temperature was below -30 ℃. Furthermore, the use of an efficient SAC is critical for the performance enhancement of the ASAHP. Choi et al. [18] designed an ASAHP with a transverse triangular obstacle SAC, and the maximum increase in COP was 8.57%. Safijahanshahi and Salmanzadeh [21] applied transpired SAC to the ASAHP system, and the results show that a 1 m^2 collector could assist a 1 kW ASHP and the transpired SAC significantly reduced the electricity consumption of ASHP. Ural et al. [22] compared the ASAHP with the novel transpired SAC and the traditional flat-plate SAC. Results show that the novel transpired SAC exhibited superior performance with the COP of 5.11 and exergy efficiency improvement of 56%.

The previous researches demonstrate that the ASAHP is efficient and desirable for residential heating. The solar irradiance, outdoor air temperature, indoor temperature, south wall covered area of TSAC and heating load of rural residences are important factors affecting the system performance. And the optimal working modes under variable operating conditions are essential for the system energy efficiency improvement. However, to the authors' knowledge, researches on the different working modes and operation strategy of ASAHP are rare.

As the SAC is the key component of the ASAHP, it is crucial to propose an efficient SAC suitable for ASAHP. The triangular solar air collector (TSAC) has been proven to be a promising SAC [23], and in this paper, a novel TSAC assisted air source heat pump

(TSAHP) for rural residence heating is proposed. The mathematical model of the TSAC and the ASHP were established and validated by experiments. Three working modes of the TSAHP were investigated, and the effects of the solar irradiance, outdoor temperature, indoor temperature, south wall covered area of TSAC and heating load on the performance of the three working modes were analyzed. The optimal working mode under varying operating conditions was resolved and the boundary equations of different working modes were fitted. Finally, the proposed optimal operation strategy was applied to a TSAHP system. Comparative analysis was conducted to verify the superiorities of the TSAHP system over the traditional ASHP system under typical meteorological conditions. The main contributions of this study include: (1) A novel TSAHP system was proposed. (2) Three working modes of TSAHP were investigated. (3) The operation strategy of TSAHP was obtained by the optimal working mode distribution diagram.

2. System description

The TSAHP system is divided into the TSAC unit and the ASHP unit connected by the air duct, as shown in Fig. 1. The TSAC with tilted glass cover can penetrate more solar irradiance. The perforated corrugated absorbers have high solar irradiance absorption and heat transfer efficiency. The circulated air is drawn into the TSAC through the upper air duct, heated by the perforated corrugated absorbers, and discharged through the lower air duct. The upper air duct is connected to the indoor and outdoor, and the lower air duct is jointed to the indoor and the ASHP evaporator and the condenser. The ASHP contains a rotary-piston variable frequency compressor,

finned-tube evaporator and condenser, and capillary as the throttle. The system runs under the three working modes, namely, the preheating, parallel and series mode. According to the specific operation strategy, the shifting of different working modes can be realized by controlling the air valves (AV). The three working modes of the TSAHP system were described as follows:

On preheating mode, valves 2 and 3 are opened, whereas valves 1, 4 and 5 are closed. Outdoor air is drawn into the TSAC, heated by solar irradiance and enters the evaporator through the air duct. In this working mode, the ASHP evaporation temperature and COP increase, and the frosting problem is alleviated.

On parallel mode, valves 1 and 5 are opened, whereas valves 2, 3 and 4 are closed. The TSAC and ASHP are both independent for heating. In addition, on parallel mode, the outlet air velocity of TSAC is set at 2 m/s and the air temperature is required to exceed 25 ℃ [20].

On series mode, valves 1 and 4 are opened, whereas valves 2, 3 and 5 are closed. The indoor air flows through the TSAC and the condenser successively. After being heated twice, the air is sent into the room for heating. On this working mode, the TSAHP system can simultaneously utilize solar energy and air energy.

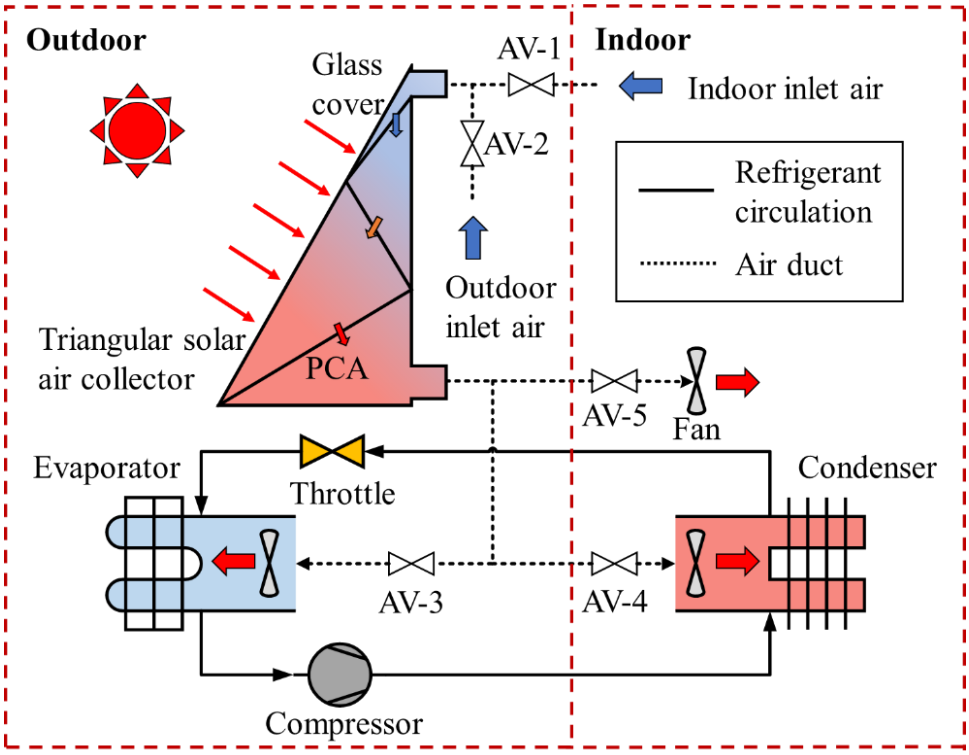

Fig. 1 Schematic of the TSAHP system.

3. Methods

3.1. Mathematical model

3.1.1. Assumptions

In this section, a mathematical model is developed to analyze the operation strategy of the TSAHP. The following assumptions are considered for simplicity:

a) The circulating air is considered to be ideal gas, and the velocity is uniformly distributed within each cross-section of the TSAHP system.

b) Except for the refrigerant, the thermal properties of the system components are temperature independent.

c) Heat losses in air ducts and refrigerant circulation pipes are ignored.

d) The compression process is considered as isentropic compression.

e) The refrigerant is isenthalpic at the inlet and outlet of the throttle.

3.1.2. The TSAC model

The TSAC consists of a glass cover, perforated corrugated absorbers, recirculation air and insulation housing. The convective and radiation heat transfer between the four parts of the TSAC and the outdoor environment are considered, and energy conservation equations are established. The heat transfer schematic of TSAC is shown in Fig. 2.

Energy conservation equation for the glass cover:

$$Q_{\text{sol.gc}} + Q_{\text{conv.gc-od}} + Q_{\text{conv.gc-air}} + Q_{\text{rad.gc-od}} + Q_{\text{rad.gc-ab}} + Q_{\text{rad.gc-ho}} = 0 \quad (1)$$

Energy conservation equation for the perforated corrugated absorbers:

$$Q_{\text{sol.ab}} + Q_{\text{conv.ab-air}} + Q_{\text{conv.hole}} + Q_{\text{rad.ab-gc}} + Q_{\text{rad.ab-ho}} + Q_{\text{rad.ab-ab}} = 0 \quad (2)$$

Energy conservation equation for the insulation housing:

$$Q_{\text{conv.ho-air}} + Q_{\text{rad.ho-gc}} + Q_{\text{rad.ho-ab}} + Q_{\text{rad.ho-ho}} = 0 \quad (3)$$

Energy conservation equation for the recirculation air:

$$Q_{\text{conv.ho-air}} + Q_{\text{conv.hole}} + Q_{\text{conv.gc-air}} + Q_{\text{conv.ab-air}} + Q_{\text{u.air}} = 0 \quad (4)$$

Kirchhoff's irradiance law is adopted to solve the radiation heat transfer between the TSAC solid parts, including $Q_{\text{rad.gc-ab}}$, $Q_{\text{rad.gc-ho}}$, $Q_{\text{rad.ab-ho}}$, $Q_{\text{rad.ab-ab}}$, and $Q_{\text{rad.ho-ho}}$. Other heat transfer elements were calculated as follows [23]:

$$Q_{\text{sol.gc}} = a_{\text{gc}} A_{\text{gc}} I_{\text{gc}} \quad (5)$$

$$Q_{\text{conv.gc-od}} = h_{\text{conv.gc-od}} A_{\text{gc}} \left(T_{\text{od}} - T_{\text{gc}} \right) \quad (6)$$

$$Q_{\text{conv.gc-air}} = h_{\text{conv.gc-air}} A_{\text{gc}} \left(T_{\text{air}} - T_{\text{gc}} \right) \quad (7)$$

$$Q_{\text{rad.gc-od}}=h_{\text{rad.gc-od}}A_{\text{gc}}\left(\sqrt[4]{\frac{1+\cos\beta_{\text{gc}}}{2}\varepsilon_{\text{sky}}+\frac{1-\cos\beta_{\text{gc}}}{2}}T_{\text{od}}-T_{\text{gc}}\right) \tag{8}$$

$$Q_{\text{sol.ab}}=a_{\text{ab}}A_{\text{ab}}I_{\text{ab}} \tag{9}$$

$$Q_{\text{conv.ab-air}}=h_{\text{conv.ab-air}}A_{\text{ab}}\left(1-P_{\text{h}}\right)\left(T_{\text{air}}-T_{\text{ab}}\right) \tag{10}$$

$$Q_{\text{conv.hole}}=h_{\text{conv.hole}}A_{\text{ab}}\frac{4d_{\text{ab}}P_{\text{h}}}{D}\left(T_{\text{ab}}-T_{\text{air}}\right) \tag{11}$$

$$Q_{\text{conv.ho-air}}=h_{\text{conv.ho-air}}A_{\text{ho}}\left(T_{\text{ho}}-T_{\text{air}}\right) \tag{12}$$

$$Q_{\text{u.air}}=m_{\text{air}}c_{\text{p.air}}\left(T_{\text{air.out}}-T_{\text{air.in}}\right) \tag{13}$$

The heat transfer coefficients $h_{\text{conv.gc-od}}$ and $h_{\text{rad.gc-od}}$ are proposed by Watmuff et al. [24] and Kumar et al. [25], $h_{\text{conv.gc-air}}$, $h_{\text{conv.ab-air}}$ and $h_{\text{conv.ho-air}}$ are proposed by Leon and Kumar [26], and $h_{\text{conv.hole}}$ is proposed by Vandecker et al. [27].

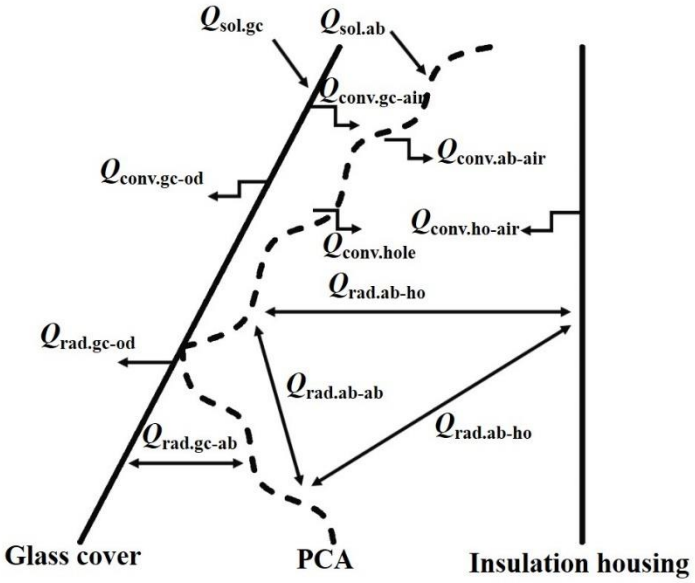

Fig.2. The heat transfer schematic of TSAC.

3.1.3. The compressor model

The varying states of the refrigerant within the ASHP are shown in Figure. 3. Points 1 and 2 correspond to the compressor suction and discharge vapor conditions, processes 9 - 1 and 2 - 3 represent the isenthalpic pressure drop of the compressor

suction and the discharge pipes, respectively. The refrigerant pressure drops in the evaporator and condenser are considered, but the liquid pipe pressure drop is ignored and regarded as a part of the idealized throttle, which corresponds to an isenthalpic process 6 - 7.

The ASHP model is established based on energy conservation and semi-empirical correlations. In the compressor, the refrigerant compression process can be simplified as isentropic, and the isentropic exponent and volumetric efficiency formula are applied to derive the compressor model [28].

$$m_{\mathrm{ref}} = \rho_1\left(9.17\times10^{-6} f_{\mathrm{comp}}\eta_{\mathrm{v}} - 2.43\times10^{-11}\left(P_2 - P_1\right)\right) \tag{14}$$

$$\eta_{\mathrm{v}} = 1 - 0.0317\left(\left(P_2/P_1\right)^{1/\kappa} - 1\right) \tag{15}$$

$$\kappa = \frac{\ln\left(P_2/P_1\right)}{\ln\left(\rho_\kappa/\rho_1\right)} \tag{16}$$

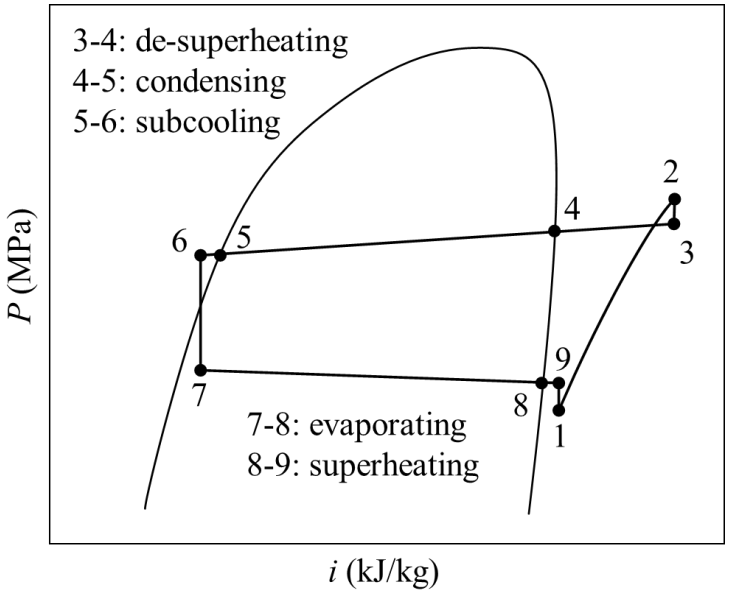

Fig.3. Pressure enthalpy diagram of refrigerant.

The pressure drops of the compressor suction and discharge pipes can be formulated as follows [29]:

$$\Delta P_{\text{sph}} = \lambda_{\text{sph}} \frac{L}{d_{\text{in}}} \frac{G_{\text{ref}}^{\ 2}}{2\rho_{\text{avg}}} \tag{17}$$

$$\frac{1}{\sqrt{\lambda_{\text{sph}}}} = 1.74 - 2\log\left(\frac{2e}{d_{\text{in}}} + \frac{18.7}{\text{Re}\sqrt{\lambda_{\text{sph}}}}\right) \tag{18}$$

$$\text{Re} = \frac{G_{\text{ref}} d_{\text{in}}}{\mu_{\text{avg}}} \tag{19}$$

The compressor input power includes the motor inverter loss W_{inv} and the shaft power W_{e}. The empirical formula of the compressor shaft power, and the compressor inverter loss are referred from Ref [21].

$$W_{\text{comb}} = W_{\text{e}} + W_{\text{inv}} \tag{20}$$

$$W_{\text{e}} \times \eta_{\text{comb}} = m_{\text{ref}} \left(\frac{\kappa}{\kappa - 1}\right)\left(\frac{P_1}{\rho_1}\right)\left(\left(\frac{P_2}{P_1}\right)^{\frac{\kappa-1}{\kappa}} - 1\right) \tag{21}$$

$$\eta_{\text{comb}} = -0.145 + 1.213\exp - 0.04P_1 \tag{22}$$

$$W_{\text{inv}} = 0.0153W_{\text{e}} + 23.4 \tag{23}$$

3.1.4. The evaporator and condenser model

The models of evaporator and condenser are developed using the number of transfer unit (NTU) method of the finned-tube heat exchanger. As shown in Figure 3, the evaporator and condenser are divided into 5 regions. The energy balance equation of each region (taking a-b as an example) is as follows [30]:

$$Q_{\text{a-b}} = m_{\text{ref}}\left(i_{\text{b}} - i_{\text{a}}\right) = \varepsilon_{\text{a-b}} C_{\text{a-b}} (T_{\text{air}} - T_{\text{ref.a}}) \tag{24}$$

The heat exchange efficiency $\varepsilon_{\text{a-b}}$ of the single-phase region including de-superheating, subcooling and superheating region is [30]:

$$\varepsilon_{\text{a-b}} = 1 - \exp\left(NTU_{\text{a-b}}^{\ 0.22}\left(\exp\left(-\frac{C_{\text{a-b.min}}}{C_{\text{a-b.max}}} NTU_{\text{a-b}}^{\ 0.78}\right) - 1\right)\right) \tag{25}$$

$$NTU_{\text{a-b}} = \frac{UA_{\text{a-b}}}{C_{\text{a-b.min}}} \tag{26}$$

$$C_{\text{a-b.min}} = y_{a-b} m_{air} \min(c_{\text{p.air}}; \left| \frac{i_{\text{b}} - i_{\text{a}}}{T_{\text{ref.b}} - T_{\text{ref.a}}} \right|) \tag{27}$$

$$C_{\text{a-b.max}} = y_{a-b} m_{air} \max(c_{\text{p.air}}; \left| \frac{i_{\text{b}} - i_{\text{a}}}{T_{\text{ref.b}} - T_{\text{ref.a}}} \right|) \tag{28}$$

The heat exchange efficiency of the condensing and evaporating region can be formulated as [30]:

$$\varepsilon_{\text{a-b}} = 1 - \exp\left(\frac{-UA_{\text{a-b}}}{C_{\text{a-b}}} \right) \tag{29}$$

$$C_{\text{a-b}} = y_{a-b} m_{air} c_{\text{p.air}} \tag{30}$$

In this work, the evaporator and condenser are finned-tube exchangers, and the total thermal resistance can be derived as follows:

$$\frac{1}{UA} = \frac{1}{\eta_{\text{tf}} h_{\text{out}} A_{\text{out}}} + \frac{\ln\left(d_{\text{out}}/d_{\text{in}}\right)}{2\pi L k} + \frac{1}{h_{\text{in}} A_{\text{in}}} \tag{31}$$

The total finned efficiency η_{tf} is proposed by McQuiston and Parker [29]. The convective heat transfer coefficient on the outside surface of the finned-tube exchanger h_{out} is presented by Gary and Webb [31], and the convective heat transfer coefficient of the inside surface h_{in} is proposed by Zakula et al. [32].

The pressure drop formulas in the de-superheating and superheating regions are the same as those in the compressor suction and discharge pipes, while the pressure drops in the condensing and evaporating regions are calculated as follows [33]:

$$\Delta P_{\text{tph}} = \left(\frac{\lambda_{\text{tph}} L \left(v_{\text{out}} + v_{\text{in}}\right)}{d_{\text{in}}} + \left(v_{\text{out}} - v_{\text{in}}\right) \right) G_{\text{ref}}^{\ 2} \tag{32}$$

$$\lambda_{\text{tph}} = 0.00506 \,\text{Re}^{-0.0951} K_{\text{ref}}^{\ 0.1554} \tag{33}$$

$$K_{\text{ref}} = \frac{\Delta x i_{\text{lv}}}{Lg} \tag{34}$$

The fan power consumptions of the evaporator and condenser can be calculated as follows [32]:

$$W_{\text{fan}} = 1.48 \times 10^{-7} \omega^{2.832} \tag{35}$$

$$\omega = 1602.6 m_{\text{air}} v_{\text{air}} + 57.8 \tag{36}$$

3.2. System evaluation

The heating load of the rural residence, Q_{h} can be calculated by Energy Plus. On the preheating mode, the heating load is met by the condenser heat transfer rate, while on the parallel and series modes, the heating load is met by both condenser heat transfer rate and the net heat gain of the TSAC. To evaluate the performance of the TSAHP system, the total input power W_{t} and COP are calculated by:

$$W_{\text{t}} = W_{\text{comb}} + W_{\text{fan}} \tag{37}$$

$$COP = Q_{\text{h}} / W_{\text{t}} \tag{38}$$

3.3. Numerical calculation method

At the beginning of the TSAHP numerical calculation process, boundary conditions are input, including the indoor temperature T_{id}, outdoor temperature T_{od}, solar irradiance I_{gc}, mass flow of refrigerant m_{ref}, condenser heat transfer rate Q_{con}, area ratio of subcooling region $y_{5\text{-}6}$, and degree of superheat $\Delta T_{8\text{-}9}$. The TSAHP model is divided into the TSAC, evaporator, condenser and compressor sub-models. To solve the TSAC model, the inlet temperature of the recirculation air is determined based on the boundary conditions and working modes. The outlet temperature of the

recirculated air is obtained by solving the TSAC model, which is also used to calculate the heating capacity of the rural residence or as the boundary conditions of the evaporator or condenser model, according to the corresponding working modes. Then the evaporator heat transfer rate Q_{eva} is assumed, the trial values i_6 and P_2 are assigned, and the evaporator, compressor and condenser model are solved successively to obtain the calculated value of condenser heat transfer rate $Q_{con.new}$. Finally, the Q_{eva} is iteratively calculated by the genetic algorithm to make Q_{con} approximate to $Q_{con.new}$. The numerical method is realized by Python environment and the refrigerant physical parameters are calculated by the REFPROP package. The flowchart of the numerical method is shown in Fig. 4.

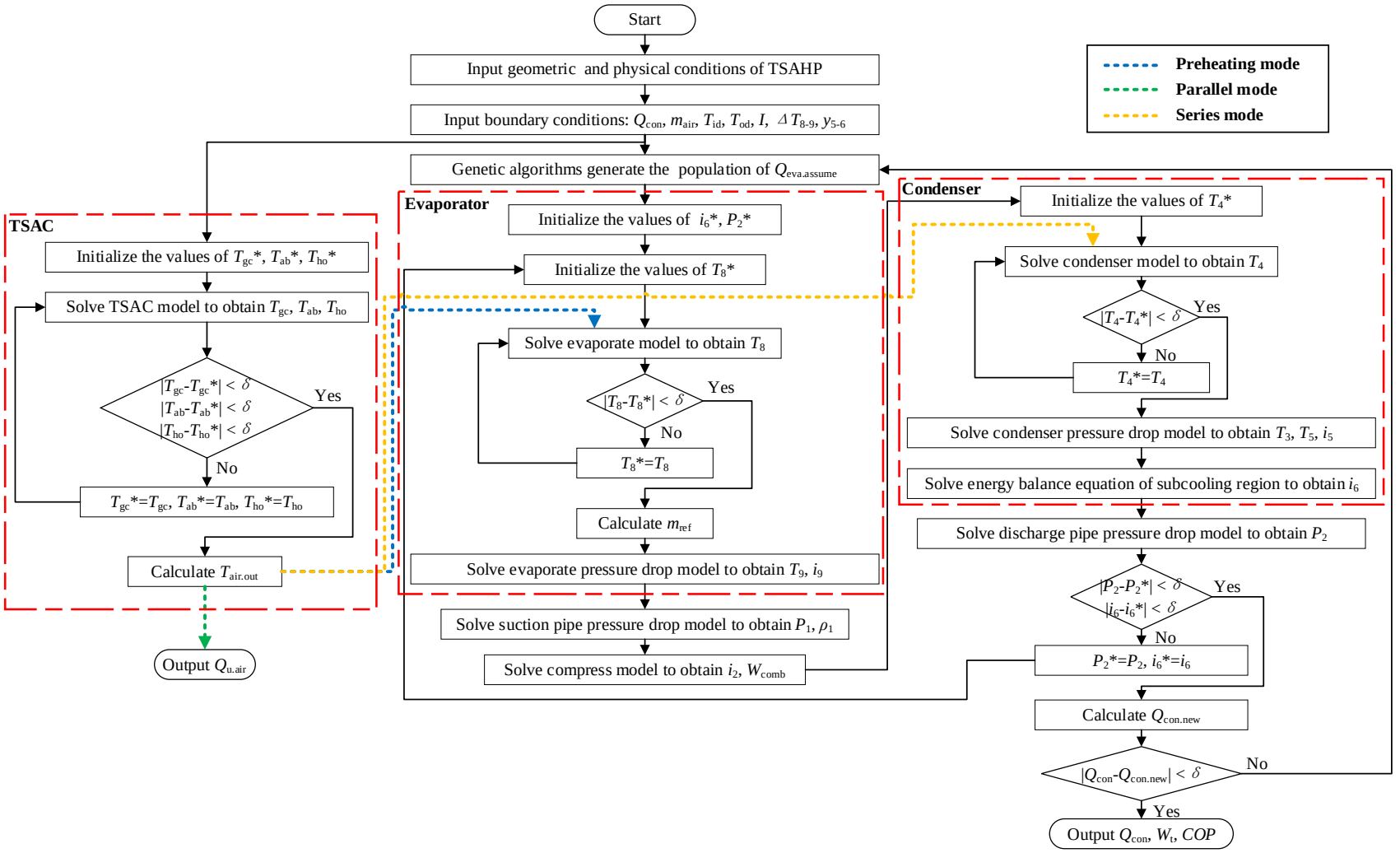

Fig.4. Flowchart of the numerical method.

4. Result and discussion

4.1. Model validation

As shown in Figure 5, the TSAC test system consists of a TSAC, a thermostatic air tank, which provides a specified inlet temperature, and a draught fan, which varies the airflow rate. The inclination angle of the TSAC glass cover is 60°. The absorber is a folding installed perforated corrugated absorber. During the test, the inlet air temperature $T_{\text{air.in}}$, outlet air temperature $T_{\text{air.out}}$, air mass flow m_{air}, solar irradiance I_{gc} and outdoor temperature T_{od} were monitored. The technical characteristics of the tested TSAC and parameters of measuring instruments are detailed in Ref [23].

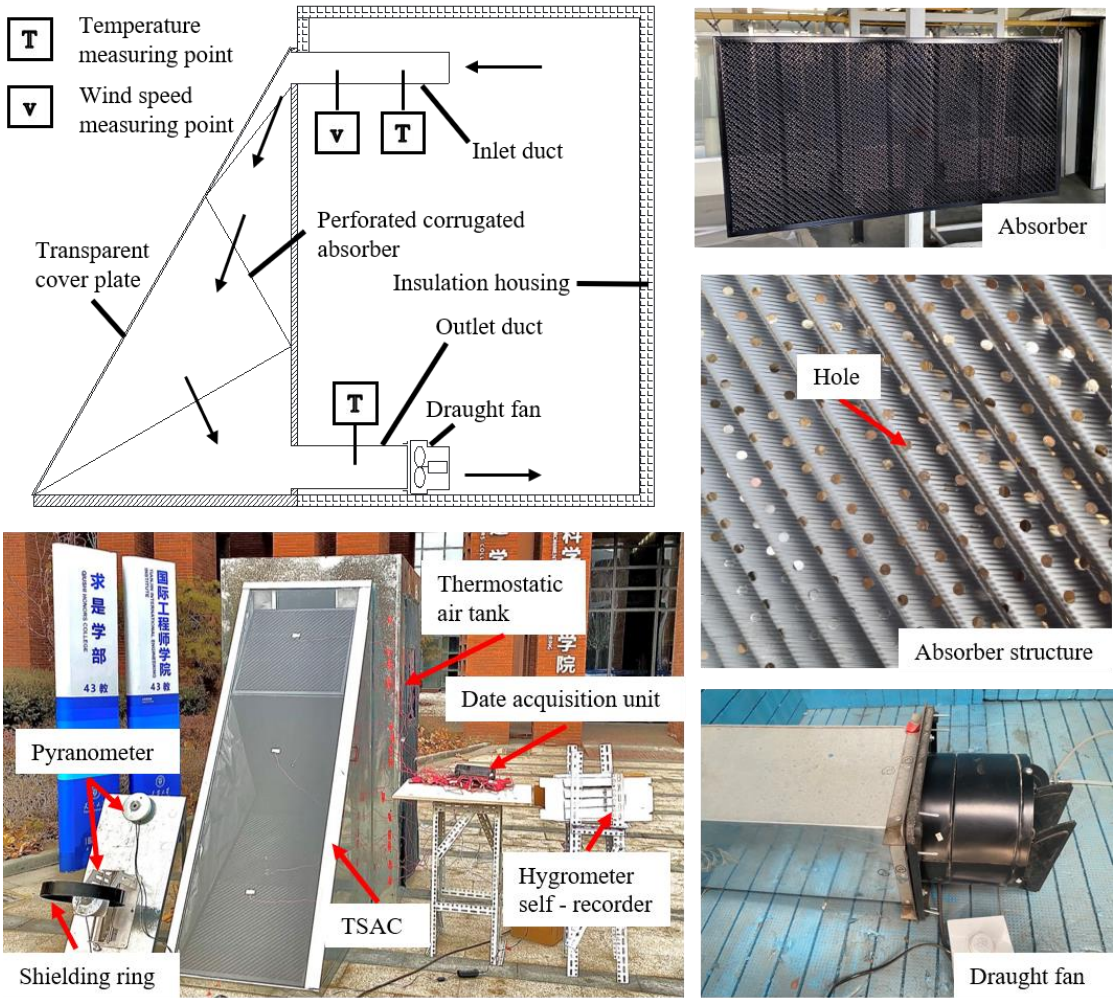

Fig.5. Sketch and photograph of experimental rig for TSAC

Comparison of the temperature rise ΔT_{air} and the net heat gain $Q_{u.air}$ of the recirculation air at different air mass flow m_{air} are depicted in Fig. 6. The average errors of the temperature rise and the net heat gain are 0.4 ℃ and 24.1 W, the average and maximum relative errors are 4.6% and 10.8%. The maximum error occurs at the minimum air mass flow, and the error decreases when the air mass flow is large, as the velocity of the circulating air is uniformly distributed in each cross-section of the TSAC. The tested and predicted values for temperature rises and net heat gain indicates satisfactory consistencies, which shows the reliability of the presented TSAC model.

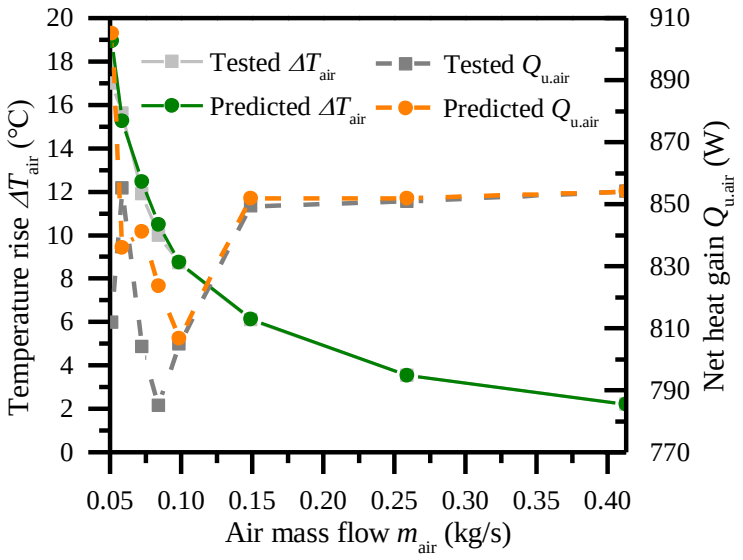

Fig. 6. The comparison between tested and predicted results at different mass flow rate.

The ASHP model has been validated in the research of Safijahanshahi and Salmanzadeh by comparing the tested and predicted values of 77 different working conditions [21]. The errors of key parameters are evaluated, and the absolute errors of evaporation temperature are less than 2 ℃, the average relative errors of compressor

outlet pressure and COP are 3% and 7%, respectively. The reasonable agreement between tested and predicted vital parameters illustrates the accuracy of the ASHP model.

4.2. Effects of the key parameters

The key parameters of the TSAHP system include solar irradiance, outdoor temperature, indoor temperature, south wall covered area of TSAC and heating load of rural residence. In order to investigate the effects of single parameter, the alternative parameters were set at standard values: I_{gc} = 600 W/m^2, T_{od} = 0 ℃, T_{id} = 18 ℃, A_{TSAC} = 2 m^2, Q_h = 2 kW.

The effects of solar irradiance on the performance of three working modes are shown in Fig.7. With the rise of solar irradiance, the evaporator outlet temperature on the three working modes increases linearly as the net heat gain of TSAC increases. On the preheating mode, the TSAC inlet temperature is outdoor temperature, as the TSAC has little heat loss and large net heat gain, and the heated circulating air is directly blown into the evaporator, thus the evaporator outlet temperature is the highest. But the evaporator outlet temperature is always lower than the outdoor temperature, indicating that the net heat gain of the TSAC is fully utilized. On series and parallel mode, the net heat gain of the TSAC reduces the heat transfer demand by the condenser, thus reducing the compression ratio and increasing the evaporation temperature and evaporator outlet temperature. When the solar irradiance is 600 W/m^2, under the parallel mode, the outlet temperature of the circulating air reaches the threshold temperature (25 ℃), which makes the parallel mode enabled. Compared with the series mode, the TSAC flow rate

and heat loss of the parallel mode are minor, therefore the net heat gain and evaporator outlet temperature are slightly higher. With the rise of solar radiation, the COPs under the series and parallel modes increase rapidly, as the increase of solar irradiance improves the net heat gain of the TSAC and reduces the required heat transfer rate of the condenser and the compression ratio. Under the parallel mode, the net heat gain of the TSAC is larger, and the condensation temperature is not increased as that under the series mode, therefore, the COP is higher. When the solar irradiance is lower than 200 W/m^2, the COP of the preheating mode is larger than that of the series mode, due to the largest net heat gain of the TSAC. When the solar irradiance is higher than 600 W/m^2, the parallel mode can operate with the maximum COP. When the solar irradiance is intermediate, the COP of the series mode is the maximum.

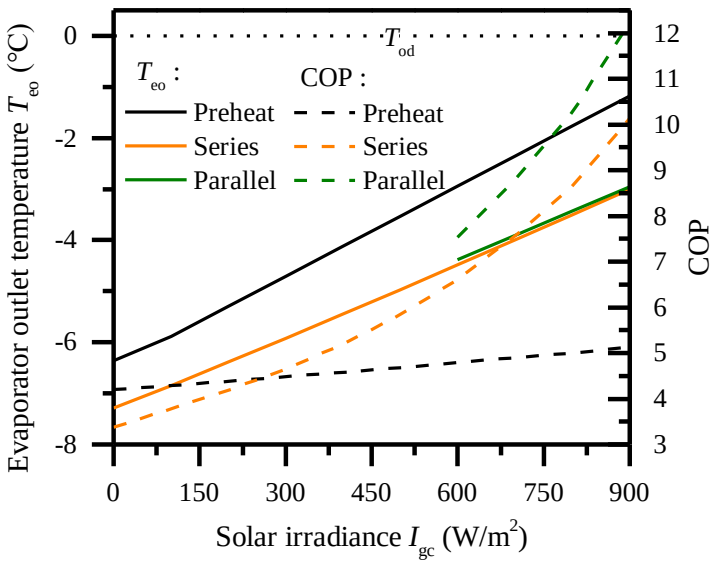

Fig. 7. The effect of solar irradiance on evaporator outlet temperature and COP.

Fig. 8 shows the effect of the outdoor temperature on the performance of the three working modes. With the increase of outdoor temperature, the inlet temperature of the

evaporator raises, leading to the increase of the evaporation temperature and evaporator outlet temperature of the three working modes. The rise of the evaporation temperature reduces the compressor compression ratio, thus COP also increases. When the outdoor temperature is above 0 ℃, the parallel mode reaches the threshold and is enabled, as the TSAC heat loss decreases and the net heat gain increases. At low outdoor temperatures, the heat loss of TSAC under the preheating mode is little, and the net heat gain of the TSAC is much higher than that under the series and parallel modes. While the advantage of preheating mode is weakened by the high outdoor temperature, as COP of series and parallel mode increased faster with the increase of outdoor temperature. When the outdoor temperature increases from - 12 to 12 ℃, the difference of COP between the series and preheating mode ascends from 0.67 to 4.63. According to the above analysis, the preheating mode is superior at lower outdoor temperatures, while the parallel and series modes are preferable at higher outdoor temperatures.

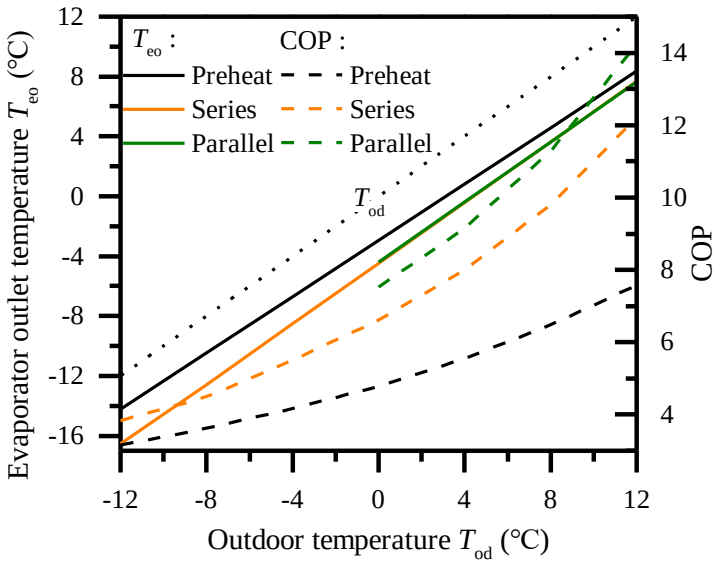

Fig. 8. The effect of outdoor temperature on evaporator outlet temperature and COP.

The effects of the indoor temperature on the performance of the three working modes are illustrated in Fig. 9. At different indoor temperatures, the inlet temperatures of the evaporator under the three working modes remain unchanged. Under the preheating mode, the condenser inlet temperature, and the condensation temperature raises thus the evaporation temperature and the evaporator outlet temperature increase. But the increase of the condensation temperature results in the rise of the compression ratio, as the COP decreases. Under the series and parallel modes, the inlet temperature and heat loss of the TSAC increase, which leads to the decrease of the net heat gain and the increase of the condenser heat transfer rate. To the combined influence of the condensation temperature and condenser heat transfer rate increase, evaporator outlet temperature and the COP decrease, and the COP decreases more rapidly than that under the preheating mode. Therefore, the preheating mode is superior at higher indoor temperatures due to little TSAC heat loss. In addition, the parallel mode can be enabled at the indoor temperature up to 18 ℃.

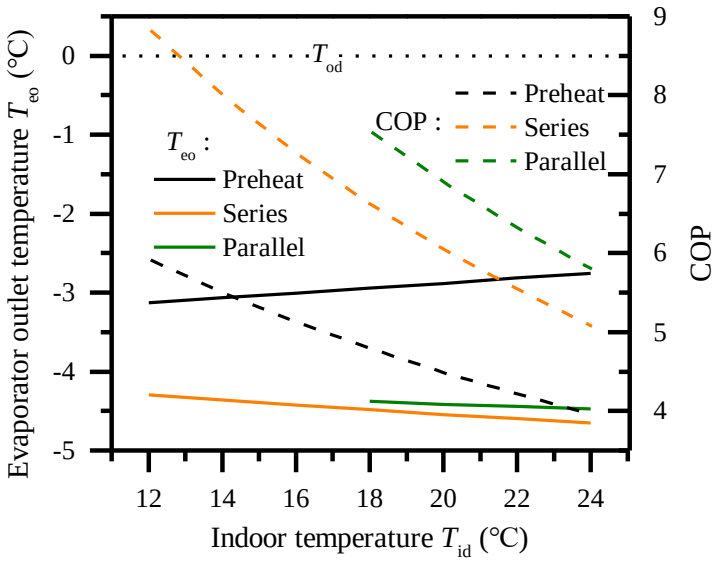

Fig. 9. The effect of indoor temperature on evaporator outlet temperature and COP.

Fig. 10 shows the effect of the south wall covered area of the TSAC on the performance of the three working modes. The TSAC can be installed on the south wall to integrate with the building envelope. Therefore, the effect of the TSAC south wall covered area rather than the heat collection area is analyzed. With the increase of the south wall covered area, the net heat gain, and the outlet temperature of the TSAC ascends. Under the preheating mode, the increase of the evaporator inlet temperature leads to the rise of the evaporation temperature and evaporator outlet temperature. With the increase of the evaporation temperature, the compression ratio decreases and the COP increases. Under the series and parallel modes, the net heat gain of the TSAC increases, thus the heat transfer rate of the condenser and compression ratio decrease, the evaporator outlet temperature and COP increase. The COPs under the series and parallel modes increase rapidly, with the south wall covered area of TSAC varying from 1 m^2 to 3 m^2, the COP under the series mode increases by 3.7, while the COP under the preheating mode increases by 0.6. This indicates that the series mode reduces the compression ratio by reducing the heat transfer rate of the condenser, which is more effective than the preheating mode to reduce the compression ratio by increasing the evaporation temperature.

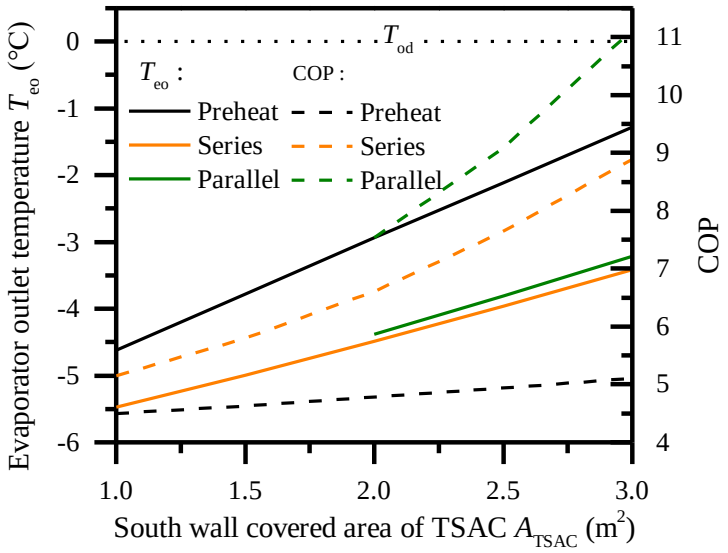

Fig. 10. The effect of south wall covered area on evaporator outlet temperature and COP.

The effect of the heating load on the performance of the three working modes is illustrated in Fig. 11. With the increase of the heating load, the compression ratio increases, thus the evaporator outlet temperature and COP decrease. The COPs of the series and parallel modes decrease rapidly, as the ratio of the net heat gain of the TSAC to the heat transfer rate of the condenser descends, and the heating load is mainly satisfied by the heat transfer of the condenser. It is noticed that when the heating load is lower than 1.1 kW, the evaporator outlet temperature under the preheating mode is higher than the outdoor temperature, which indicates that the net heat gain of the TSAC is not fully exploited. Therefore, under the preheating mode, if the heating load is small for a long time, the evaporator outlet should be connected to the TSAC inlet, and the circulating air enters the TSAC directly from the evaporator outlet to be heated.

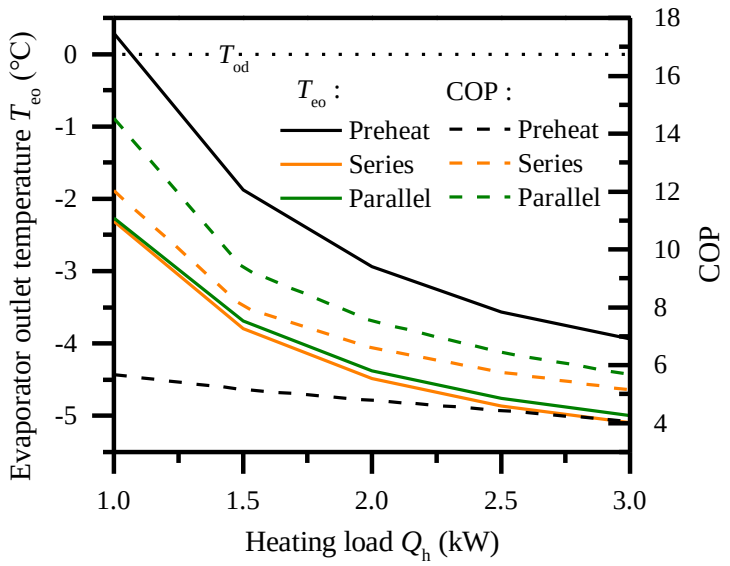

Fig. 11. The effect of heating load on evaporator outlet temperature and COP.

4.3. Optimal working mode distribution

Among the above parameters, solar irradiance and outdoor temperature vary frequently in a wide range, which are the main factors affecting TSAHP performance. The distribution of the optimal working modes under different solar irradiance and outdoor temperature is shown in Fig. 12. A certain working mode region represents that the COP of the TSAHP system under this working mode is the largest at the corresponding solar irradiance and outdoor temperature, and the boundaries between the two working modes indicate that the COPs of the two working modes are the same. According to the above analysis, the optimal working mode shifts from the preheating to series and parallel mode with the increase of solar irradiance. As the outdoor temperature increases, the distribution areas of the parallel mode and series mode as the optimal working mode increases, while the preheating mode decreases. At the boundaries of the two operating modes, the solar irradiance and the outdoor temperature

correlates to each other linearly. To determine the optimal working mode of the TSAHP system under different solar irradiance and outdoor temperature, the two boundaries are fitted.

Boundary equation of the parallel and series modes:

$$I_{gc} = -7.6167T_{od} + 606.2 \tag{39}$$

Boundary equation of the series and preheating modes:

$$I_{gc} = -11.908T_{od} + 255.1 \tag{40}$$

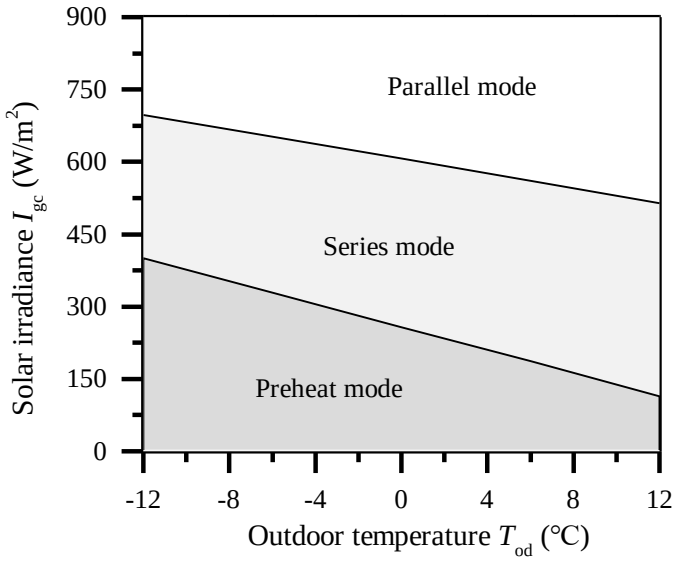

Fig. 12. The optimal working mode distribution based on meteorological parameters.

Fig. 13 shows the effect of the (a) indoor temperature, (b) south wall covered area of TSAC and (c) heating load of rural residence on optimal working mode distribution. As shown in Fig. 13(a), with the indoor temperature from 14 ℃ to 22 ℃, the boundary between the parallel and the series mode moves downwards, since the indoor temperature under the parallel mode is the inlet temperature of the TSAC, and a higher inlet temperature makes it easier for the TSAC outlet temperature to reach the threshold.

As shown from the previous analysis, if the parallel mode reaches the threshold, it will be enabled, and its COP is higher than that under the series mode. Under the series mode, the increase of the indoor temperature results in an increase of the TSAC inlet temperature and heat loss, and the advantage of the low TSAC heat loss under the preheating mode is amplified, thus the boundary between the series and preheating mode moves upwards. It is noticed that the boundaries are parallel at different indoor temperatures, which indicates that the indoor temperature only changes the offsets of the boundary equations. The indoor temperature is negatively correlated with the offsets of the boundary equations under the parallel and series modes, and positively correlated with the offsets of the boundary equations under the series and preheating modes. As shown in Fig. 13(b), with the south wall covered area of the TSAC varying from 1 m^2 to 3 m^2, the boundary between the parallel and series mode moves downwards, as the increase of area raises the net heat gain and outlet temperature of the TSAC under the parallel mode to reach the threshold. The increased area ascends the TSAC outlet temperature, which increases the net heat gain under the series mode or the evaporation temperature under the preheating mode. According to the previous analysis, rising the net heat gain is more effective in reducing the compression ratio, therefore the boundary between series and preheating mode also moves downwards. In addition, the south wall covered area of TSAC is negatively related to the offsets and slopes of the boundary equations. As shown in Fig. 13(c), the heating load of the rural residence only affects the boundary between the series and preheating modes, and the boundary moves upwards with the increase of the heating load, as the ratio of the net heat gain of the

TSAC under the series mode to the heat transfer rate of the condenser descends. The heating load of the rural residence is positively related to the offsets and slopes of the boundary equations under the series and preheating modes. Based on the effect of the indoor temperature, the south wall covered area of the TSAC and the heating load of the rural residence, the boundary equations are modified as follows:

Modified boundary equation of the parallel and series modes:

$$I_{gc}=\left(1.1797A_{TSAC}-10.113\right)T_{od}+\frac{e^{11.784}}{T_{id}^{1.673}A_{TSAC}^{0.824}} \tag{41}$$

Modified boundary equation of the series and preheating modes:

$$I_{gc}=\frac{-e^{0.876}Q_h^{0.229}}{A_{TSAC}^{0.195}}T_{od}+\frac{e^{1.679}T_{id}^{0.869}Q_h^{0.196}}{A_{TSAC}^{0.207}} \tag{42}$$

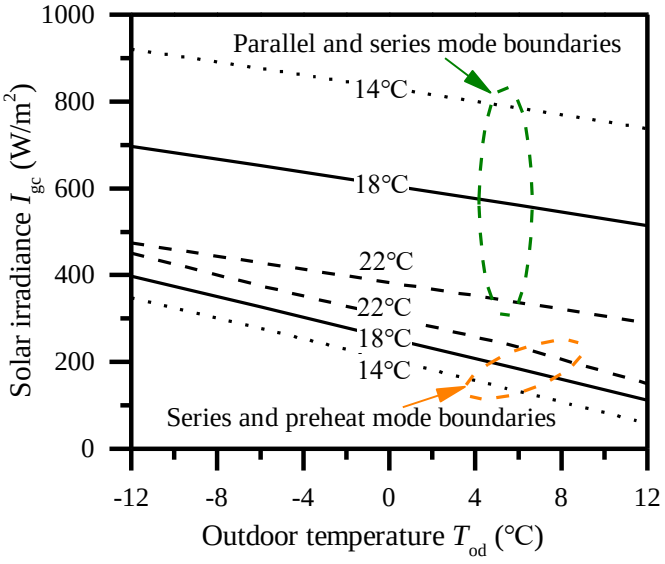

(a)

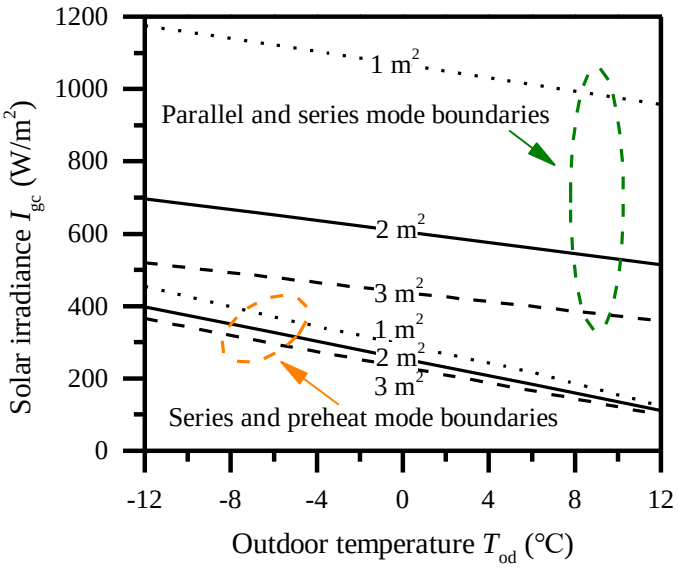

(b)

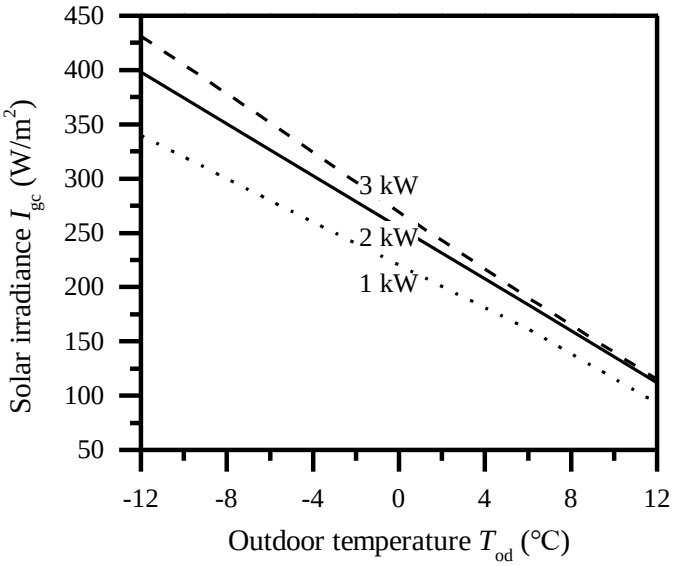

(c)

Fig. 13. The effect of parameters on optimal working mode distribution.

4.4. Application of the optimal working mode

To analyze the heating performance of the TSAHP system under the optimal working mode, it is compared with the traditional ASHP, and the ASHP and TSAC independent operation (ASHP-T). The meteorological parameters of Jan 22 and Jan 7

in a typical meteorological year in Tianjin, China (39.98 °N, 117.38 °E), and the heating load of a 50 m^2 rural residence under corresponding meteorological parameters are adopted for simulation. As shown in Fig. 14, Jan 22 is a sunny day with high solar irradiance and outdoor temperature, and a low heating load of rural residence. The maximum solar irradiance is 825.1 W/m^2 at 12:00, and the maximum outdoor temperature is 5.9 ℃. In contrast, Jan 11 is a cloudy day with a maximum outdoor temperature of 0.7 ℃ and a maximum solar irradiance of 460.8 W/m^2 at 13:00. In addition, the indoor temperature and south wall covered area of TSAC are maintained constant, which is 18 ℃ and 2 m^2, respectively.

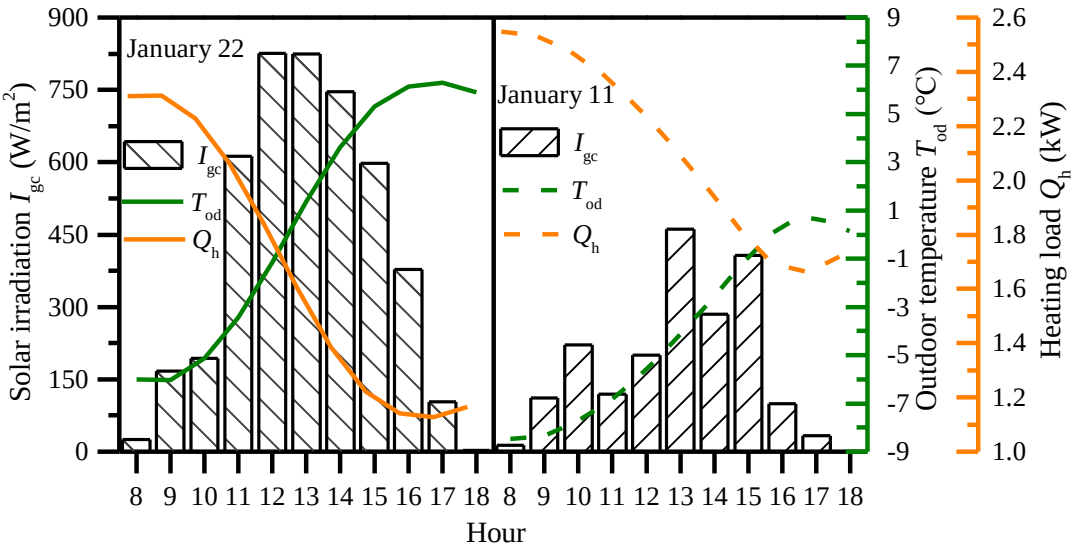

Fig. 14. The meteorological parameters of Jan 22 and Jan 11.

According to the modified boundary equations, the hourly optimal working mode is determined, and the COP of the TSAHP system is calculated by the corresponding working mode model. As shown in Fig. 15(a), the COP of the traditional ASHP heating is mainly affected by the outdoor temperature. With the increase of the outdoor

temperature, the heating load decreases and the COP increases, and the maximum COP is 5.5 at 17:00. When the TSAC and ASHP operate independently, the TSAC reaches the threshold and operates for four hours from 12:00 to 15:00. However, when the TSAHP system is under the optimal working mode, the TSAC operates from 8:00 to 18:00, including five hours of preheating mode at low solar irradiance, two hours of series mode at intermediate solar irradiance, and four hours of parallel mode at high solar irradiance. Compared with the traditional ASHP heating, the average COP of the TSAHP system under the optimal working mode is increased by 64.4%, and the power consumption is reduced by 1.2 kWh. The meteorological parameters at 11:00 in Ref [21] are close to this research, and COP at 11:00 in this research is improved by 40.8%, while that in Ref [21] is only improved by 15.6%. As Ref [21] is still on the preheating mode at 11:00, which is not the optimal working mode under corresponding operating conditions. As shown in Fig. 15(b), the COP of the traditional ASHP heating is low, as the outdoor temperature is low, and the heating load is high. It is noticed that the TSAC can’t operate independently during the whole period due to the low solar irradiance. While for the TSAHP system under the optimal working mode, the TSAC can operate from 8:00 to 18:00, including nine hours of preheating mode and three hours of series mode, and the average COP is increased by 6.2%, and the power consumption is reduced by 0.3 kWh. Even on a cloudy day, the maximum COP of TSAHP is 5.18 under the optimal working mode, which is higher than 5.11 in the Ref [22].

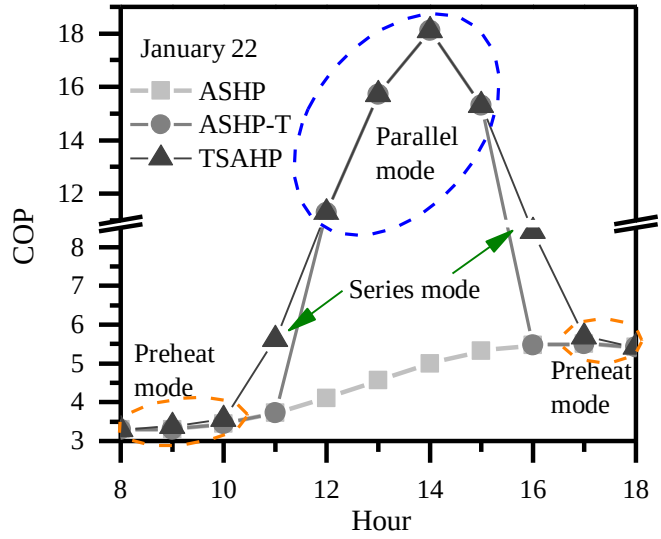

(a)

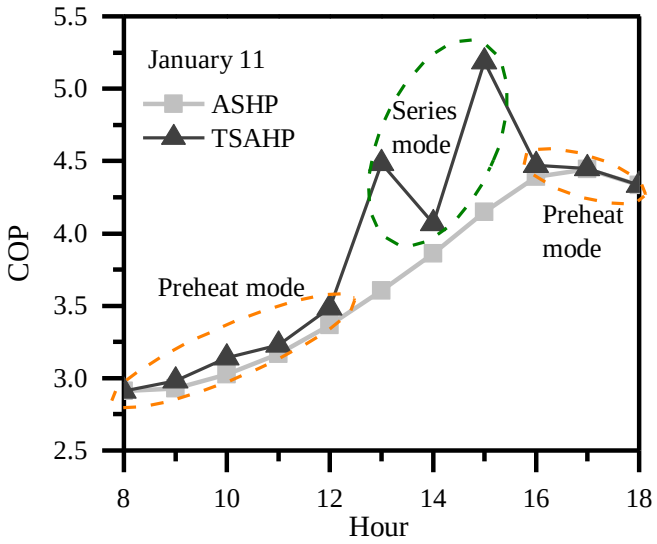

(b)

Fig. 15. The application and comparison of optimal working mode.

5. Conclusions

To improve the heating efficiency of the ASHP, a novel triangular solar air collector assisted air source heat pump (TSAHP) is proposed. Three working modes of the TSAHP system are investigated, and the mathematical models are established and

verified. The performances of the TSAHP on three working modes are analyzed under different operational and meteorological parameters. The optimal operation mode distribution of the TSAHP is obtained and the boundary equations are fitted. The main conclusions are drawn as follows:

(1) Solar irradiance is an important factor affecting the performance of TSAHP. With the increase of solar irradiance, the optimal working mode is shifted from the preheating to series and parallel.

(2) The boundary equations of the optimal working mode distribution are linear equations of the solar irradiance and outdoor temperature. The indoor temperature is only related to the offsets of the boundary equations, while the south wall covered area of TSAC is related to the offsets and slopes, and the heating load only affects the boundary equation of series and preheating mode. The optimal working mode of TSAHP can be determined effectively by the modified boundary equation.

(3) The TSAHP is more energy-efficient than traditional ASHP and largely extends the operating time of TSAC, which enhances the utilization rate of solar energy. On sunny days, the average COP of the TSAHP in the optimal operation mode increases by 64.4%. Even on cloudy days, the average COP can be increased by 6.2%. The performance of TSAHP under optimal working mode is obviously better than that under single preheating mode in literature.

The results of this study contribute to promoting the application of solar air collector assisted air source heat pump (TSAHP) in the heating of rural residence. In

our future works, the energy, exergy, economic and environmental of the proposed TSAHP will be analyzed and evaluated, and the exploitation of the preheating mode for alleviating the frosting problem of the evaporator will be investigated.

Acknowledgement

This work was supported by the National Key R&D Program of China (No. 2020YFD1100304-06).

References

[1] Deng M, Ma R, Lu F, Nie Y, Li P, Ding X, Yuan Y, Shan M, Yang X. Techno-economic performances of clean heating solutions to replace raw coal for heating in Northern rural China. Energy & Buildings. 2021; 240:110881.

https://doi.org/10.1016/j.enbuild.2021.110881

[2] Reiners T, Gross M, Altieri L, Wagner H J, Bertsch V. Heat pump efficiency in fifth generation ultra-low temperature district heating networks using a wastewater heat source. Energy. 2021; 236:121318.

https://doi.org/10.1016/j.energy.2021.121318

[3] Wu Z, You S, Zhang H, Wang Y, Jiang Y, Liu Z, Sha L, Wei Shen. Experimental investigations and multi-objective optimization of an air-source absorption heat pump for residential district heating. Energy Conversion and Management. 2021; 240:114267.

https://doi.org/10.1016/j.enconman.2021.114267

[4] Fan Y, Zhao X, Han Z, Li J, Badiei A, Akhlaghi Y G, Liu Z. Scientific and

technological progress and future perspectives of the solar assisted heat pump (SAHP) system. Energy. 2021; 229:120719.

https://doi.org/10.1016/j.energy.2021.120719

[5] Cai J, Li Z, Ji J, Zhou F. Performance analysis of a novel air source hybrid solar assisted heat pump. Renewable Energy. 2019; 139:1133-1145.

https://doi.org/10.1016/j.renene.2019.02.134

[6] Yao J, Zheng S, Chen D, Dai Y, Huang M. Performance improvement of vapor-injection heat pump system by employing PVT collector/evaporator for residential heating in cold climate region. Energy. 2021; 219:119636.

https://doi.org/10.1016/j.energy.2020.119636

[7] Ma K, Wang Z, Li X, Wu P, Li S. Structural optimization of collector/evaporator of direct-expansion solar/air-assisted heat pump. Alexandria Engineering Journal. 2021; 60:387-392.

https://doi.org/10.1016/j.aej.2020.08.039

[8] Song Z, Ji J, Cai J, Zhao B, Li Z. Investigation on a direct-expansion solar-assisted heat pump with a novel hybrid compound parabolic concentrator/photovoltaic/fn evaporator. Applied Energy. 2021; 299:117279.

https://doi.org/10.1016/j.apenergy.2021.117279

[9] Hao W, Zhang H, Liu S, Mi B, Lai Y. Mathematical modeling and performance analysis of direct expansion heat pump assisted solar drying system. Renewable Energy. 2021; 165:77-87.

https://doi.org/10.1016/j.renene.2020.11.008

[10]Fan C, Yan G, Yu J. Thermodynamic analysis of a modified solar assisted ejector-compression heat pump cycle with zeotropic mixture R290/R600a. Applied Thermal Engineering. 2019; 150:42-49.

https://doi.org/10.1016/j.applthermaleng.2019.01.011

[11]Liu Z, Wang Q, Wu D, Zhang Y, Yin H, Yu H, Jin G, Zhao X. Operating performance of a solar/air-dual source heat pump system under various refrigerant flow rates and distributions. Applied Thermal Engineering. 2020; 178:115631.

https://doi.org/10.1016/j.applthermaleng.2020.115631

[12]Liu M, He Y, Zhang H, Su H, Zhang Z. The feasibility of solar thermal-air source heat pump water heaters in renewable energy shortage regions. Energy. 2020; 197:117189.

https://doi.org/10.1016/j.energy.2020.117189

[13]Agrebi S, Chargui R, Tashtoush B, Guizani A. Comparative performance analysis of a solar assisted heat pump for greenhouse heating in Tunisia. International Journal of Refrigeration. 2021; 00225-5.

https://doi.org/10.1016/j.ijrefrig.2021.06.004

[14]Simonetti R, Molinaroli L, Manzolini G. Experimental and analytical study of an innovative integrated dual-source evaporator for solar-assisted heat pumps. Solar Energy. 2019; 194:939-951.

https://doi.org/10.1016/j.solener.2019.10.070

[15]Long J, Xia K, Zhong H, Lu H, Yongga A. Study on energy-saving operation of a combined heating system of solar hot water and air source heat pump. Energy Conversion and Management. 2021; 229:113624.

https://doi.org/10.1016/j.enconman.2020.113624

[16]Cai J, Ji J, Wang Y, Huang W. Operation characteristics of a novel dual source multi-functional heat pump system under various working modes. Applied Energy. 2017; 194:236-246.

http://dx.doi.org/10.1016/j.apenergy.2016.10.075

[17]Treichel C, A.Cruickshank C. Energy analysis of heat pump water heaters coupled with air-based solar thermal collectors in Canada and the United States. Energy. 2021; 221:119801.

https://doi.org/10.1016/j.energy.2021.119801

[18]Choi H U, Kim Y B, Son C H, Yoon J I, Choi K H. Experimental study on the performance of heat pump water heating system coupled with air type PV/T collector. Applied Thermal Engineering. 2020; 178:115427.

https://doi.org/10.1016/j.applthermaleng.2020.115427

[19]Kegel M, Tamasauskas J, Sunye R, Langlois A. Assessment of a solar assisted air source and a solar assisted water source heat pump system in a Canadian household. Energy Procedia. 2012; 30:654-663.

doi: 10.1016/j.egypro.2012.11.074

[20]Xu W, Liu C, Li A, Li J, Qiao B. Feasibility and performance study on hybrid air

source heat pump system for ultra-low energy building in severe cold region of China. Renewable Energy. 2020; 146:2124-2133.

https://doi.org/10.1016/j.renene.2019.08.079

[21] Safijahanshahi E, Salmanzadeh M. Performance simulation of combined heat pump with unglazed transpired solar collector. Solar Energy. 2019; 180:575-593.

https://doi.org/10.1016/j.solener.2019.01.038

[22] Ural T, Kecebas A, Guler O V. Thermodynamic performance evaluation of a heat pump system with textile based solar air heater for heating process. Applied Thermal Engineering. 2021; 191:116905.

https://doi.org/10.1016/j.applthermaleng.2021.116905

[23] Jiang Y, Zhang H, Wang Y, You S, Wu Z, Fan M, Wang L, Wei S. A comparative study on the performance of a novel triangular solar air collector with tilted transparent cover plate. Solar Energy. 2021; 227:224-235.

https://doi.org/10.1016/j.solener.2021.08.083

[24] Watmuff J.H., Charters W.W.S., Proctor D. Solar and wind induced external coefficients - solar collectors. COMPLES. 1977; 2-56.

[25] Kumar A, Bhagoria J L, Sarviya R M. Heat transfer and friction correlations for artificially roughened solar air heater duct with discrete W-shaped ribs. Energy Conversion and Management. 2009; 50:2106-2117.

doi:10.1016/j.enconman.2009.01.025

[26] Leon M A, Kumar S. Mathematical modeling and thermal performance analysis of

unglazed transpired solar collectors. Journal of Energy Storage. 2007; 81:62-75. doi:10.1016/j.solener.2006.06.017

[27] Vandecker G.W.E., Hollands K.G.T., Brunger A.P. Heat-exchange relations for unglazed transpired solar collectors with circular holes on a square or triangular pitch. Solar Energy. 2001; 71:33-45.

[28] Armstrong P R, Jiang W, Winiarski D, Katipamula S, Norford L K, Willingham R A. Efficient Low-Lift Cooling with Radiant Distribution, Thermal Storage, and Variable-Speed Chiller Controls—Part I: Component and Subsystem Models. HVAC&R Research. 2014; 25:09-54.

http://dx.doi.org/10.1080/10789669.2009.10390842

[29] ASHRAE. 2009 ASHRAE Handbook-Fundamentals. At-lanta, GA: American Society of Heating, Refrigerating and Air-Conditioning Engineers, Inc. 2009.

[30] McQuiston F C, Parker J D, Spitler J D. Heating, ventilating, and air conditioning: analysis and design. John Wiley & Sons, Inc.1982.

[31] Gray D L, Webb R L. Heat transfer and friction correlation for plate finned-tube heat exchangers having plain fins. Proceedings of 8th International Heat Transfer Conference. 1986; 6:2745–2750.

[32] Zakula T, Gayeski N T, Armstrong P R, Norford L K. Variable-speed heat pump model for a wide range of cooling conditions and loads. HVAC&R Research. 2011; 670-691.

http://dx.doi.org/10.1080/10789669.2011.607745

[33]Choi J Y, Kedzierski M A, Domanski P A. Generalized pressure drop correlation for evaporation and condensation in smooth and micro-fin tubes. Proc. Report NISTIR 6333. Gaithersburg, MD: National Institute of Standards and Technology, USA. 2001.